NUMERICAL INVESTIGATION OF THE MAGNUS EFFECT ON DIMPLED SPHERES

Nikolaos Beratlis
Mechanical and Aerospace Engineering
Arizona State University
Tempe, AZ, USA
nikos.beratlis@gmail.com

Elias Balaras
Department of Mechanical
and Aerospace Enginering
George Washington University
Washington, DC, USA
balaras@gwu.edu

Kyle Squires
Mechanical and Aerospace Enginering
Arizona State University
Tempe, AZ, USA
squires@asu.edu

ABSTRACT

An efficient finite-difference, immersed-boundary, Navier-Stokes solver is used to carry out a series of simulations of spinning dimpled spheres at three distinct flow regimes: subcritical, critical and supercritical. Results exhibit all the qualitative flow features that are unique in each regime, namely the drag crisis and the alternation of the Magnus effect.

INTRODUCTION

Golf ball aerodynamics are of particular importance not only due to the quest for improved performance of golf balls but also because of the fundamental phenomena associated with the drag reduction due to dimples. Dimples are known to lower the critical Reynolds number at which a sudden drop in the drag is observed. Figure 1, for example, shows the drag coefficient, C_D, as a function of the Reynolds number, $Re = UD/\nu$, (where D is the diameter of the golf ball, U the velocity and ν the kinematic viscosity of the air) for a golf ball and for spheres with various degrees of roughness [Achenbach (1972); Bearman & Harvey (1976)]. It can be seen that dimples are more effective in lowering the critical Reynolds number compared to sand-roughened spheres with grain size k equal to the dimple depth d. In addition, dimples have the benefit of not increasing drag considerably in the supercritical region (the region after the minimum in C_D is reached), although that minimum value of C_D is not as low as that of a smooth sphere.

It is generally believed that dimples cause the laminar boundary layers to transition to turbulence, energizing the near wall flow and adding momentum, which helps overcome the adverse pressure gradient and delay separation. Recently Choi *et al.* (2006) carried out a series of experiments on dimpled spheres to clarify the mechanism of drag reduction caused by dimples. Using hot-wire anemometry they measured the streamwise velocity within individual dimples and showed that the boundary layer separates locally within the dimples. They concluded that turbulence is generated by a shear layer instability which causes momentum transfer of high speed fluid towards the surface of the sphere. Further support for this mechanism was provided by recent direct numerical simulations (DNS) by Smith *et al.* (2010). In their work, flow visualization identified the formation of thin shear layers at the leading edge of the dimples, which become unstable and are effective in energizing the near-wall flow.

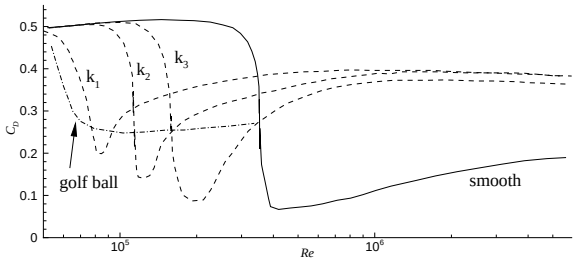

Figure 1. Variation of C_D vs Re for a smooth sphere Achenbach (1972), –; spheres with sand-grained roughness Achenbach (1972), $--$ ($k_1 = k/d = 1250 \times 10^{-5}$, $k_2 = 500 \times 10^{-5}$, $k_3 = 150 \times 10^{-5}$); golf ball Bearman & Harvey (1976), $\cdot-$.

When a sphere or golf ball is spinning around an axis perpendicular to the flow, a significant lift force is also generated. Robins (1805) showed in the 18th century that the spherical shots fired from bent gun barrels experience a lift force. A century later Magnus (1853) employed a spinning cylinder to demonstrate the existence of lift and attributed this phenomena on the Bernoulli's principle. When a cylinder spins it imparts velocity on the side moving with the flow and removes

velocity from the side moving against the flow. The higher velocity on one side means lower pressure which creates a lift force in the direction of the side spinning against to the side spinning with the flow. This phenomena is commonly termed the Magnus or Robbins effect. It wasn't until the introduction of boundary-layer theory by Prandlt in 1904 that a better explanation was given for the Magnus effect. It is now understood that lift is generated by the asymmetric separation of the boundary layer on opposite sides of a cylinder or a sphere.

Davies (1949) carried out experiments in which spinning golf balls and smooth spheres were dropped inside a wind tunnel. He estimated the lift on the balls by measuring the drift of the golf ball on the landing spot. The Reynolds number was 88×10^3 and the dimensionless spin rate $a = \omega D/2U$ varied up to 0.55, where ω is the rotational speed in rpm. The interesting point in his observations was the existence of a negative Magnus effect for the case of a smooth sphere and $a < 0.35$, that is lift in the direction opposite to that predicted by the Magnus effect. He attributed the negative Magnus effect on the possibility that the effective Reynolds number on each side of the sphere is different creating a distinct pressure distribution on each side that results in negative lift.

Bearman & Harvey (1976) used large scale models of golf balls with spherical and hexagonal dimples attached to two thin wires. A motor was placed inside the hollow shells of the ball to enable spinning at the desired rotational speeds. The Reynolds number varied from 3.8×10^4-2.4×10^5 and a from 0-2. They generally observed that as the spin rate increases so do the lift and drag, although for the lowest Re and for spin rates less than $a \sim 0.23$ negative lift was observed. They speculated that the generation of negative lift was due to the fact that the boundary layer on the side spinning with the flow remained laminar while the one on the side spinning against the flow was tripped into a turbulent state. However, no visual or quantitative information was provided to support this conjecture.

More recently several other experimental studies have been carried out on spinning golf balls in order to quantify the effect of dimples and rotation on the drag and lift [i.e. Stanczak *et al.* (1998); Aoyama (1998)]. The main problem with the experiments, however, is the inherent limitation to measure quantities near and within the dimples when the golf ball is spinning. Computational studies can bridge this gap and provide detailed spatial and temporal information for spinning golf balls. The recent large-eddy simulations (LES) by Aoki *et al.* (2010) and DNS by Smith *et al.* (2010) are characteristic examples. The present study extends the work by Smith *et al.* (2010) to rotating golf balls. We will present results at four Reynolds numbers covering the subcritical, critical and supercritical flow regimes at constant rotation rate, a.

METHODOLOGIES AND SETUP

The flow around a spinning golf ball is governed by the Navier-Stokes equations for viscous incompressible flow. In the present formulation the governing equations are discretized on a structured grid in cylindrical coordinates, and the boundary conditions on the surface of the golf ball, which is not aligned with the grid lines, are introduced using an immersed-boundary method [see Yang & Balaras (2006)]. An exact, semi-implicit, projection method is used for the time advancement. All terms are treated explicitly using the Runge-Kutta 3rd order scheme, except for the viscous and convective terms in the azimuthal direction which are treated implicitly using the 2nd order Crank-Nicholson scheme [see Aksevoll & Moin (1996)]. All spatial derivatives are discretized using second-order central-differences on a staggered grid.

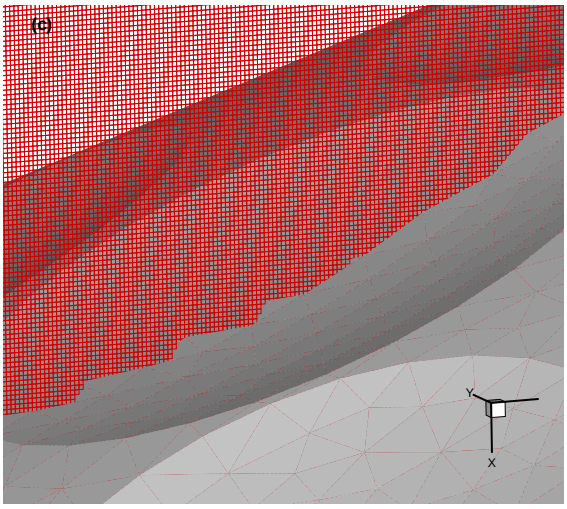

Figure 2. Typical grid resolution in a dimple.

The code is parallelized using a classical domain decomposition approach. The domain is evenly divided along the axial direction and communication between processors is done using MPI library calls. Most tasks, like the computation of the right hand side and the advancement of the velocity in the predictor and corrector steps, can be performed independently on each processor. To facilitate that, each subdomain contains one layer of ghost cells to its left and right. The value of any variable at the ghost cells is obtained by simple 'ejection' from the neighboring subdomain, which is part of the cost of communication between processors.

We considered four different Reynolds numbers, $Re = DU/\nu$, and one dimensionless rotation rate, α. Their values were chosen in a way that all three distinct flow regimes, namely the subcritical ($Re = 1.7 \times 10^4$ and $a = 0.12568$), critical ($Re = 4.5 \times 10^4$ and $a = 0.12568$ and $Re = 6.5 \times 10^4$ and $a = 0.12568$) and supercritical ($Re = 1.7 \times 10^5$ and $a = 0.12568$) are covered (see Table 1 for a summary of the computations). The dimensional parameters for the supercritical case correspond to the velocity and rotation rate of a golf ball in flight after a typical stroke. The dimple diameter is approximately $d \sim D/10$, and the dimple depth, $h = D/160$. The details of the geometry can be found in Smith *et al.* (2010). The Eulerian grid is stretched in the axial and radial directions to resolve the key flow features. Figure 2 shows an example of the computational grid near a dimple.

For all cases the domain extends $10D$ upstream and $30D$ downstream of the golf ball (the center of the golf ball is located at $r/D = 0$, $z/D = 0$). The number of grid points used in each case is shown in Table 1. As the Reynolds number increases the grid resolution around the golf ball and total grid size increases too. For the supercritical case the resolution in the radial and axial directions is the highest of all. In par-

Case	Re	α	U_∞	ω	Grid resolution	CPU hrs/rot.	$\overline{C_d}$	$\overline{C_l}$
case 1	1.7×10^4	0.12568	5.8m/s	350rpm	$296\times102\times1002$	1800	0.454	0.0460
case 2	4.5×10^4	0.12568	15.0m/s	920rpm	$442\times502\times1502$	47000	0.362	-0.0411
case 2	6.5×10^4	0.12568	22.0m/s	1340rpm	$442\times502\times1502$	68000	0.249	0.120
case 3	1.7×10^5	0.12568	58.0m/s	3500rpm	$1000\times502\times3002$	260000	0.212	0.0215

Table 1. Summary of the simulations

ticular, at $r/D = 0.35$ and $z/D = \pm0.35$ $\Delta r \sim \Delta z = 5.0e-4$ respectively. Since the dimples at those locations are oriented at 45° from either radial or axial coordinate directions, the resolution requirements are the highest. With this arrangement there are approximately 8-9 grid cells inside the dimple and across the laminar boundary layer at those locations. As one moves towards the top of the golf ball ($r/D = 0.5$ and $z/D = 0.0$), where the dimples are aligned with the axial coordinate and the radial grid determines the wall normal resolution the number of points inside the dimple cavity is increased to 10-12. A uniform grid of 502 points is used in the azimuthal direction. The resulting grid has $760\times502\times3002$ in the radial, azimuthal and axial directions respectively. For the two cases in the critical flow regime at lower Re the grid resolution in the radial and axial directions was relaxed since the boundary layer is thicker but the number of points in the azimuthal direction was kept the same. The corresponding grid sizes together with typical CPU hours required to complete one rotation in each case can be found in Table 1.

RESULTS

Various time averaged quantities have been computed. Usually for flows with a clear periodic condition, such as the period of rotation of the golf ball, phase-averaging could be employed. However in order to converge phase-averaged statistics one would need to consider many rotations, which would make the computations prohibitively expensive even for the smallest grids. In addition, the spin rates considered in this study are small and the flow can be considered quasi-steady.

Table 1 lists the mean force coefficients for all cases. As the Reynolds number increases from $Re = 1.7\times10^4$ (subcritical) to $Re = 4.5\times10^4$ (critical) the drag coefficient, $\overline{C_d}$, decreases by 37%, from 0.45 to 0.36. A further drop of $\overline{C_d}$ to 0.25 is observed as the Reynolds number increases to $Re = 6.5\times10^4$ still in the critical regime. Finally in the supercritical flow regime the mean drag coefficient attains its lowest value of $\overline{C_d} = 0.21$. Comparison of C_d values with those of spinning and stationary golf balls from various experimental studies are shown in Figure 3a. It should be noted that the dimples in these studies are circular but the exact dimple patterns and dimple depth are different from the geometry used in the present study. Our geometry contains approximately 300 dimples with depth $h/D = 6.3\times10^{-3}$. The golf ball used by Bearman & Harvey (1976) has around 250 dimples with larger dimple depth ($h/D = 9\times10^{-3}$), while that used by Choi *et al.* (2006) has 392 dimples which are more shallow ($h/D = 4\times10^{-4}$). Due to these important differences we don't expect good quantitative agreement between our results and those in the literature. The plots in figure 3a show that for a stationary golf ball the effect of increasing the dimple depth is to accelerate the drag crisis but with a higher drag at the end of the critical (minimum $\overline{C_d}$) and in the supercritical flow regimes. When spin is added ($\alpha = 0.1$) the drag increases particularly in the critical flow regime, while in the supercritical flow regime it doesn't change significantly. Despite the differences in the dimple patterns, the present results for $\overline{C_D}$ are within the range reported in the literature.

The mean lift coefficient, $\overline{C_l}$, listed in Table 1 is considerably affected by rotation and exhibits a different dependence on Reynolds number compared to $\overline{C_d}$. While $\overline{C_l}$ is positive for three cases in the subcritical, critical and supercritical flow regimes in accordance with the Magnus-Robbins effect it becomes negative at $Re = 4.5\times10^4$. A similar observation was made by Bearman & Harvey (1976), where they reported negative $\overline{C_l}$ around the same set of Re and α parameters. A direct comparison between their experiments and our computations is shown in Figure 3b. $\overline{C_l}$ in the experiments is negative around $Re = 3.8\times10^4$, and it becomes positive around $Re = 5.0\times10^4$ and reaches a maximum at $Re = 6.0\times10^4$. In the supercritical regime $\overline{C_l}$ remains positive but decreases as a function of Re. The $\overline{C_L}$ values from our DNS are close to the experimental ones and certainly exhibit the same trend including the existence of negative lift at $Re = 4.5\times10^4$. Bearman & Harvey (1976) speculated that this behavior was due to the state of the boundary layers on the upper and lower sides of the dimpled sphere: the boundary layer on the side of the golf ball spinning with the flow remained laminar, while the other side underwent transition and remained attached longer. However, there wasn't any flow visualization or any other measurement to highlight the state of the flow near the surface of the golf ball.

DISCUSSION

Figure 4 shows the instantaneous spanwise vorticity plotted at two azimuthal planes passing through the upper and lower side of the golf ball for a subcritical ($Re = 1.7\times10^4$) and a critical ($Re = 6.5\times10^4$) case. In the former the boundary layers on the upper and lower sides of the golf ball separate and form detached shear layers, which then become unstable and shed vortices in the wake. In the latter, the flow separates locally within the dimples and local shear layers are formed

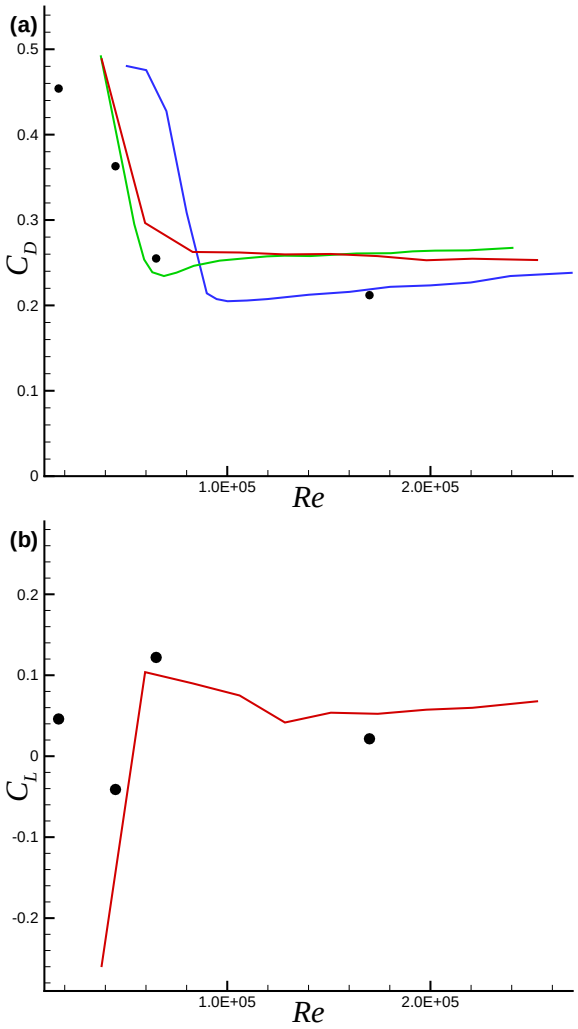

Figure 3. Mean values of a) C_D and b) C_L. Symbols are –, Choi *et al.* (2006) (h/d=4e-3, no spin); –, Bearman & Harvey (1976) (h/d=9e-3, no spin); –, Bearman & Harvey (1976) (h/d=9e-3, spin $\alpha = 0.1$); •, present DNS results (h/d=6.3e-3, spin $\alpha = 0.12568$).

above the dimples energizing the flow and eventually delaying the mean flow separation. These phenomena are similar to ones observed in stationary golf balls and have been discussed in detail in an earlier paper by Smith *et al.* (2010). The main difference in the rotating cases is that separation occurs at different angles at the upper and lower parts of the golf ball, and it is directly affected by the local structure of the boundary layers. For the case of $Re = 6.5 \times 10^4$, for example, the boundary layer on the upper side stays attached longer and local separation and transition of the shear layer starts at approximately one dimple after $\theta = 90^\circ$. On the lower side, however, local separation and transition starts earlier at one dimple before $\theta = 90^\circ$. The exact point where instabilities are triggered will vary during one rotation depending on the dimple pattern and the way dimples are aligned with the flow but in general transition occurs earlier on the lower side. This can be attributed to the difference in the local Reynolds number between the parts of the golf ball spinning with and against

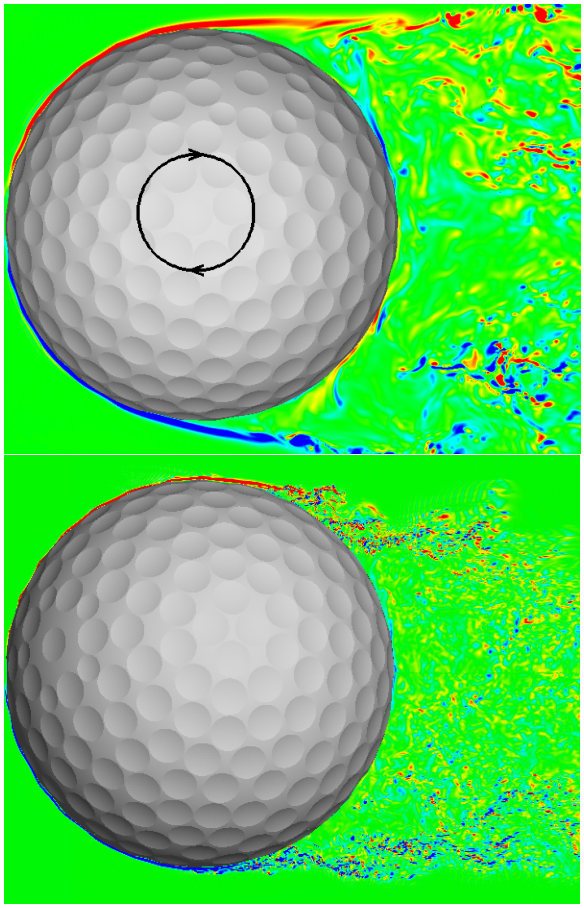

Figure 4. Contours of instantaneous spanwise vorticity at selected azimuthal planes highlighting the relative separation of the boundary layers on the upper and lower sides. The golf ball spins in the clockwise direction with $\alpha = 0.125$. $Re = 1.7 \times 10^4$ (top), and $Re = 6.5 \times 10^4$ (bottom).

the flow, which is higher in the latter case and therefore more prone to instabilities.

In addition, rotation has a profound effect in the wake structure at the back of the golf ball. At the higher Reynolds number, for example, in Figure 4 the vortical structures that are shed from the shear layer on the upper side are seen to follow the golf ball more around the back than the vortical structures on the lower side. To better understand why this happens let us consider a smooth sphere spinning in the clockwise direction in a quiescent flow. Due to viscous diffusion a clockwise rotating flow will be created around the sphere. The flow is axisymmetric around the axis of rotation so the tangential pressure gradient is zero while a radial pressure gradient exists pushing towards the center of the sphere exists. In the case of a golf ball a similar secondary flow is expected to be created by the spin. Structures that form on the upper side near the top of the golf ball are therefore convected by the secondary rotating flow around the back and towards the surface of the golf ball while structures that form on the lower side near the top of the golf ball are convected towards the front of the ball. The effect of the convection by the secondary flow is conveniently illustrated by comparing the mean spanwise

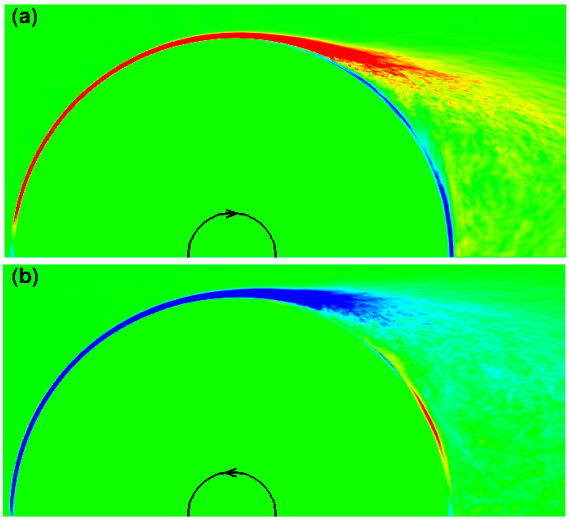

Figure 5. Contours of instantaneous spanwise vorticity at a plane passing through a) the upper side of the golf ball spinning with the flow for the case with $Re = 6.5 \times 10^4$ and $\alpha = 0.125$ and b) the lower side the golf ball spinning against the flow (inverted for comparison purposes) for the case with $Re = 4.5 \times 10^4$ and $\alpha = 0.125$.

vorticity between $Re = 4.5 \times 10^4$ and $Re = 6.5 \times 10^4$ shown in figure 5. For the $Re = 4.5 \times 10^4$ case the local Re on the lower side of the golf ball is approximately 5.1×10^4 while for the $Re = 6.5 \times 10^4$ case the local Reynolds number on the upper side of the golf ball is approximately $Re = 5.7 \times 10^4$. Since the local Reynolds numbers are very close to each other one would expect the flow dynamics and mean vorticity to be very similar too if the effects of convection by the spin were not important. However the mean vorticity on the part of the golf ball spinning with the flow curls more around the back of the golf ball than on the part spinning against the flow. Therefore convection by the secondary rotating flow is important for the set of parameters chosen in the present study.

The subcritical case at $Re = 4.5 \times 10^4$ is of particular interest due to fact that net negative lift is generated. Figure 6 shows contours of the instantaneous spanwise vorticity at two azimuthal planes passing through the upper and lower sides of the golf ball. On the upper side the boundary layer separates near the top of the golf ball forming a shear layer that is seen to undergo a Kelvin-Helmholtz type instability. A clear pair of vortices can be identified with a braid region between them. The vortices appear to break down quickly as they travel downstream. The behavior of the flow on the upper side is very similar to that at the subcritical regime. The main difference as Re increases from 1.7×10^4 to 4.5×10^4 is that the location of the shear layer instability has moved closer to although not yet at the surface of the golf ball. At the lower side of the golf ball the shear layer becomes unstable just above an individual dimple around $\theta = 100^\circ$. The vortices shed from the shear layer remain near the surface of the golf ball and over a few dimples as they travel downstream.

A more accurate picture of the flow dynamics on both sides of the golf ball near the separation point can be obtained by looking at the profiles of the time-averaged tangential velocity and turbulent kinetic energy k shown in figure 7. First of all the relative free stream velocity and therefore the local Reynolds number is higher on the lower side than on the upper one which explains why the shear layer on the side spinning against the flow becomes unstable earlier. In particular, peaks in k above $r/D = 0.5$ start to form as early as $\theta \sim 85^\circ$ while similar peaks on the upper side are not seen until $\theta \sim 95^\circ$. It is important to note that on the upper side the shear layer instability occurs after the flow separates while on the lower side the shear layer becomes unstable first which energizes the near wall flow and delays separation of the mean flow.

The time-averaged pressure coefficient $\overline{C_p}$ plotted in figure 8 shows that the main contribution to the drag comes from

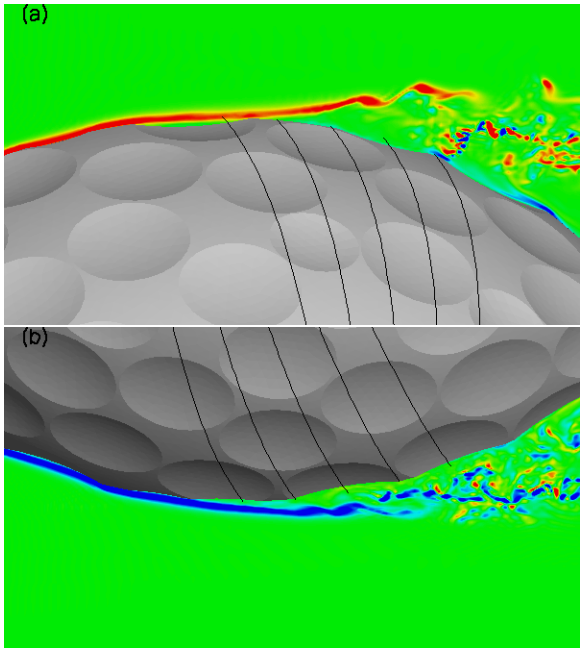

Figure 6. Contours of instantaneous spanwise vorticity at a plane passing through a) the upper side and b) the lower side of the golf ball. The solid black lines represent azimuthal arc lines starting at $\theta = 90^\circ$ and plotted every 5° for reference.

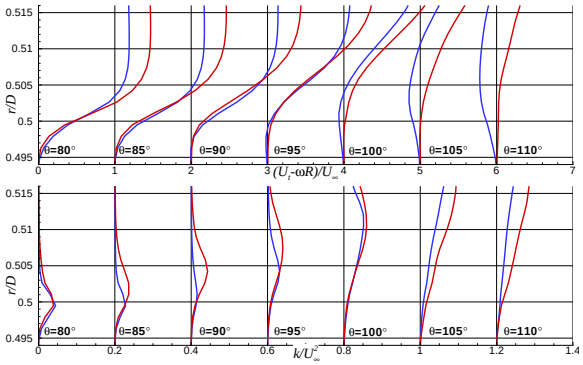

Figure 7. Profiles of time averaged : (top) tangential velocity relative to tangential spin velocity $\omega \cdot R$; (bottom) turbulent kinetic energy, at various locations for $Re = 4.5 \times 10^4$ and $\alpha = 0.126$. Colors represent: –; lower side, –; upper side.

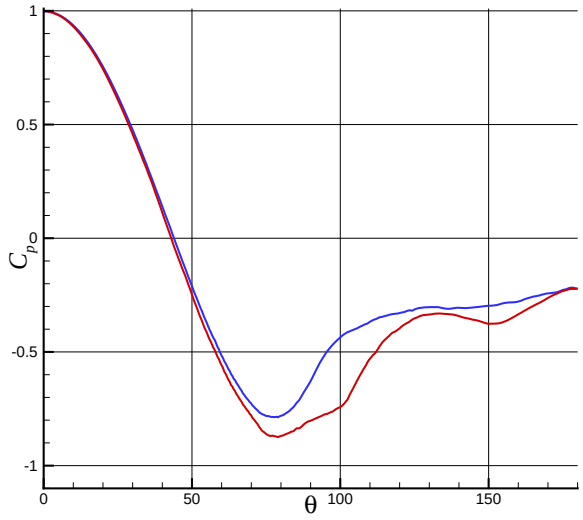

Figure 8. Time-averaged pressure coefficient $\overline{C_p}$ versus angle θ from the front of the golf ball for $Re = 4.5 \times 10^4$ and $\alpha = 0.125$. $\overline{C_p}$ is plotted at a constant radius of $0.504D$ from the center of the golf ball. Colors represent: –; lower side, –; upper side.

the point of minimum $\overline{C_p}$ around $\theta = 80^\circ$ and until the very back of the golf ball. In particular the fact that vortical structures are shed and remain closer to the surface of the golf ball on the lower side creates a lower pressure region near the wall which delays the recovery of $\overline{C_p}$ with respect to the upper side where vortical structures are shed farther away from the surface of the golf ball.

CONCLUSIONS

Direct numerical simulations of a spinning golf ball have been performed for a range of Reynolds number covering the subcritical, critical and supercritical flow regimes. The code used is a finite-difference incompressible Navier-Stokes solver that can account for a moving body through the use of an embedded boundary formulation. The code is efficiently parallelized using a domain decomposition strategy enabling computations with up to 1.1 billion grid points.

The results for drag and lift are in good agreement with various experimental studies with similar golf balls. In particular the drag drops as Re increases from the subcritical to the critical regime, and from the critical to the supercritical regime. The lift also exhibits the same qualitative features observed in experiments, namely it is positive at $Re = 1.7 \times 10^4$, $Re = 6.5 \times 10^4$ and $Re = 1.7 \times 10^5$ and negative at $Re = 4.5 \times 10^4$. It was found that spin has two principal effects, first convection of the instantaneous flow structures and mean flow in a clockwise direction and second an increase of the local Re on the side spinning against the flow relative to that spinning with the flow. The second is especially important in the $Re = 4.5 \times 10^4$ where the upper side of the golf ball exhibits features of the subcritical regime while the lower side exhibits features of the critical regime. In particular, on the upper side the boundary layer first separates and the shear layer that forms becomes unstable shedding vortices farther away from the wall while on the lower side the flow locally separates over the dimples forming thin shear layers that undergo instabilities and shed vortices which energy the near wall flow and delay separation. The resulting pressure distribution is smaller on the lower side around the region of separation giving rise to negative lift. Although previous experimental work suggested the difference in local Re on either side of the golf ball as the reason for negative lift this is the first published work that provides an in depth quantitative analysis of the mechanisms responsible for this phenomenon.

REFERENCES

Achenbach, E. 1972 Experiments on the flow past spheres at very high reynolds numbers. *Journal of Fluid Mechanics* **54**, 565.

Aksevoll, K. & Moin, P. 1996 An efficient method for temporal integration of the navier-stokes equations in confined axisymmetric geometries. *Journal of Computational Physics* **125**, 454–463.

Aoki, K., Muto, K. & Okanaga, H. 2010 Aerodynamics characteristics and flow pattern of a golf ball with rotation. *Procedia Engineering 2* pp. 2431–2436.

Aoyama, S. 1998 The row effect anomaly in the 336 octahedron dimple pattern. *Science and Golf III* .

Bearman, P. W. & Harvey, J. K. 1976 Golf ball aerodynamics. *Aeronautical Quaerterly* **27**, 112.

Choi, J., Jeon, W. & Choi, H. 2006 Mechanism of drag reduction by dimples on a sphere. *Physics of Fluids* **18**.

Davies, J. 1949 The aerodynamics of golf balls. *Journal of Applied Physics* **20**, 821–828.

Magnus, G. 1853 Ueber die abweichung der geschosse und eine auffallende erscheinung bei rotirenden korpen. *Poggendorfs Annalen der Physik und Chemie* **88**.

Robins, B. 1805 *New Principles in Gunnery*. Hutton.

Smith, C. E., Beratlis, N., Balaras, E., Squires, K. & Tsunoda, M. 2010 Numerical investigation of the flow over a golf ball in subcritical and supercritical regimes. *Intern. J. of Heat and Fluid Flow* .

Stanczak, M. N., Lemons, L. D., Beasley, D. E. & A., Liburdy J. 1998 Observations of the wake characteristics of spinning golfballs. *Science and Golf III* pp. 440–456.

Yang, J. & Balaras, E. 2006 An embedded boundary formulation for large-eddy simulation of turbulent flows interacting with moving boundaries. *Journal of Computational Physics* **15**, 12–40.